Environmental Science & Technology

pubs.acs.org/est

Article

4D Surface Reconstructions to Study Microscale Structures and Functions in Soil Biogeochemistry

Alexander D. Ost,* Tianyi Wu, Carmen Höschen, Carsten W. Mueller, Tom Wirtz, and Jean-Nicolas Audinot

Cite This: *Environ. Sci. Technol.* 2021, 55, 9384–9393

Read Online

ACCESS | Metrics & More | Article Recommendations | Supporting Information

ABSTRACT: The development of high-resolution microscopy and spectroscopy techniques has allowed the analysis of microscopic 3D objects in fields like nanotechnology and life and soil sciences. Soils have the ability to incorporate and store large amounts of organic carbon. To study this organic matter (OM) sequestration, it is essential to analyze its association with soil minerals at the relevant microaggregate scale. This has been previously studied in 2D. However, 3D surface representations would allow a variable angle and magnification analysis, providing detailed insight on their architecture. Here we illustrate a 4D surface reconstruction workflow able to locate preferential sites for OM deposition with respect to microaggregate topography. We used Helium Ion Microscopy to acquire overlapping Secondary Electron (SE) images to reconstruct the soil topography in 3D. Then we used nanoscale Secondary Ion Mass Spectrometry imaging to chemically differentiate between the OM and mineral constituents forming the microaggregates. This image was projected onto the 3D SE model to create a 4D surface reconstruction. Our results show that organo-mineral associations mainly form at medium curvatures while flat and highly curved surfaces are avoided. This method presents an important step forward to survey the 3D physical structure and chemical composition of microscale biogeochemical systems correlatively.

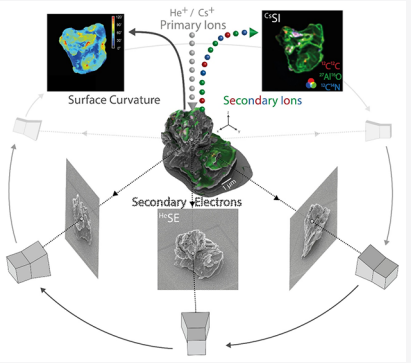

KEYWORDS: *SIMS, correlative microscopy, photogrammetry, surface reconstruction, biogeochemistry, organic matter sequestration*

1. INTRODUCTION

Correlative Microscopy (CM) has become of major importance nowadays in various domains such as nanotechnology, life, and even soil sciences. Microscopy and spectroscopy techniques are combined first to overcome limitations from each technique[1] and second to move beyond the boundaries of microscopy by data treatment.[2] Analyzing a Region of Interest (ROI) with different techniques with regards to structural and chemical properties provides complementary information and a deeper understanding about the sample.[3,4] When Secondary Ion Mass Spectrometry (SIMS) is combined with scanning or transmission electron microscopy techniques (SEM and TEM)[5] and, more recently, Helium Ion Microscopy (HIM),[6−8] CM offers high sensitivity chemical information correlated with morphology. Furthermore, correlating images obtained by different techniques using, e.g., an image overlay or the Laplace fusion method benefits the interpretation of multimodal information.[2]

SIMS is a qualitative technique for chemical surface analysis. Primary ions (e.g., Ne^+, Ga^+, Cs^+, O^-) are accelerated toward the sample, provoking the emission of secondary ions, which are collected, filtered according to their mass-to-charge ratio, and detected.[9−11] Advantages of SIMS are high sensitivity, access to the full periodic table (starting with hydrogen), distinguishability of isotopes and a high dynamic range (i.e., detectable secondary ion concentrations varying from matrix to trace elements). SIMS can be used in different modes e.g. depth profiling and imaging.

SIMS has been widely used for 3D SIMS reconstruction.[12] Sequential 2D SIMS images are obtained while eroding the surface progressively under the energetic primary ion bombardment and are then assembled into a 3D stack. However, this method does not take into account the original surface topography and its evolution during the sputtering process, since different materials and features exposed to the ion beam at different angles are sputtering at different rates.[13] The outcome is a three-dimensional block representing the ROI without any morphological information and prone to artifacts. In order to make a topography correction, AFM measurements can be performed before, as well as after,[14,15] and in-between SIMS measurements.[13,16] However, high aspect ratio particles are particularly challenging for conventional AFM due to too high scanning speed resulting in

Received: May 7, 2021
Accepted: June 9, 2021
Published: June 24, 2021

collision with the sample.[17] For this kind of samples, a photogrammetry approach has been established for 3D surface reconstruction from secondary electron (SE) images from either SEM or HIM in order to have additional information about the ROI's topography allowing a 3D view from all possible angles.[18−20]

Photogrammetry has become popular in the recent years for 3D reconstruction of macroscopic objects from images taken by a camera[21] in domains such as geography and even for soil erosion studies.[22] In general, partially overlapping images are taken around an object at different polar and azimuthal angles. The images are implemented into a photogrammetry software: features on the images are first detected and then matched at the overlapping areas from one image to another creating a point cloud by a triangulation process where matches from at least two images are required. The position of the cameras is computed and then a textured mesh is generated representing the object of interest. Therefore, the overlap from one image to another should be high to ensure enough data point detection for matching.

In recent years, Eulitz and Reiss[19] and Gontard et al.[20] have shown that this photogrammetry approach can be successfully applied to SE images of microscopic ROI's using commercial photogrammetry software specialized in reconstruction of macroscopic objects from optical images.

Vollnhals and Wirtz[18] were the first ones to extend this methodology to SE images obtained on a HIM with a specific pattern of tilt and repeating stage rotation angles. Additionally, they acquired analytical information on the same ROI by performing in situ SIMS at normal incidence and projected this SIMS information onto the 3D photogrammetric surface representations.

We note that for this photogrammetry reconstruction combined with SIMS only surface information is acquired whereas for traditional SIMS 3D reconstruction, the sample is eroded layer by layer so that volumetric chemical information is provided.[23]

Soils comprise a heterogeneous dynamic porous system that consists of mineral and organic materials of variable sizes and composition. Chemical, biological, and physical processes determine the structure and thus the function of soils, e.g., nutrient cycling, habitat for microorganisms, and soil organic carbon storage. The formation of soil aggregates, assemblages of soil minerals and organic components bound together by cementing (e.g., carbonates) and gluing agents (e.g., microbial residues) is an important control for soil functionality. Soil microaggregates (<250 μm),[24] as the smallest assemblage of mineral and organic soil constituents, are of great importance for a wide range of soil functions, besides cation exchange, soil physical stability, especially for long-term soil carbon sequestration.[25−28]

Understanding the complex 3D microscale distribution of elements and the spatial arrangement of both soil organic matter and mineral particles constituting soil microaggregates is a prerequisite to gain fundamental knowledge about the fate of soil carbon but also nutrients and pollutants in soil systems.

While Vollnhals and Wirtz[18] established the methodology of photogrammetry reconstruction combined with SIMS primarily to demonstrate its potential on basic microscopic objects (indium phosphide particles), we adapted it by appropriate workflows and applied this in the field of soil biogeochemistry.

We present here the workflow and applications of 4D surface reconstruction with two examples on soil microaggregates. Besides the illustration of the workflow and a qualitative description of a 4D surface reconstruction obtained by the analysis using the HIM-SIMS instrument, the link between the sample's chemical information delivered by nanoscale SIMS (NanoSIMS 50L) and its topography is evaluated. We provide a processing method for localization of preferential sites for organic matter (OM) sequestration with respect to the topography of soil microaggregates.

We demonstrate that correlative imaging, by a qualitative description and a deeper topographic analysis, offers the great opportunity to merge topographic and thus physical information with the distribution of elements and thus chemical data to better understand the link between soil microaggregate architecture and biogeochemical function. Furthermore, we compare two sample preparation procedures for the microscale analysis of soil microaggregates (wet and powder deposition), and make use of isotopic enrichment (^{13}C glucose) to trace the fate of freshly added OM during the formation of mineral-associated OM on the surface of microaggregates.

2. MATERIALS AND METHODS

2.1. Sample Preparation. The soil material was sampled from the upper 10 cm of the Ap horizon from a long-term agricultural research site in Puch, Germany (Cambisol according to WRB).[29] The soil was air-dried at room temperature, sieved through a 2 mm sieve and macroscopic plant residues were picked out by hand. We aimed at using state of the art approaches for the sampling and preparation of soil microaggregates, namely by the deposition of suspended microaggregates on a Si wafer and the separation of fine-sized microaggregates using sieving.[30,31] Thus, for the two presented microaggregate reconstructions, we used the most common soil sample preparation procedures and adapted them according to the intended chemical analysis.

In the first case, a 5 mL ethanol solution with a few mg of the soil sample was prepared, and some droplets were placed on a Si wafer. Due to the fine size of the deposited particles and microaggregates these were sticking to the Si carrier.

For the second microaggregate, the sample was derived from a 30 days soil incubation experiment with ^{13}C glucose (D-glucose-$^{13}C_6$, Sigma-Aldrich, ≥ 99 atom-% ^{13}C). Via dry aggregate size fractionation (adapted from Felde et al.[30]), a modified Casagrande apparatus (Mennerich Geotechnik, Hannover, Germany) equipped with three sieves was used to separate the soil material into the aggregate size fractions of <53 μm, 53−250 μm and >250 μm. As we aimed at the fine microaggregates known to store the highest relative amount of OM we used the <53 μm fraction for the microscale imaging approach. To circumvent the use of excessive water to prepare a soil suspension, we made use of condensed water films to support the fixation of microaggregates on the GaAs wafers. In brief, a few μg of the microaggregate <53 μm soil fraction was placed on a clean GaAs wafer. The wafer containing the sample was placed at −18 °C for 20 min, and subsequently, moved to room temperature. Due to the change in temperature fine water films condensed on the GaAs wafer and led to the adhesion of fine microaggregates on the surface of the wafer. This approach provides microaggregates that are fixed on the wafer and ready to be analyzed via electron microscopy and SIMS after air drying.

2.2. Helium Ion Microscopy (HIM). The Secondary Electron (SE) images were acquired in a ZEISS ORION

https://doi.org/10.1021/acs.est.1c02971
Environ. Sci. Technol. 2021, 55, 9384−9393

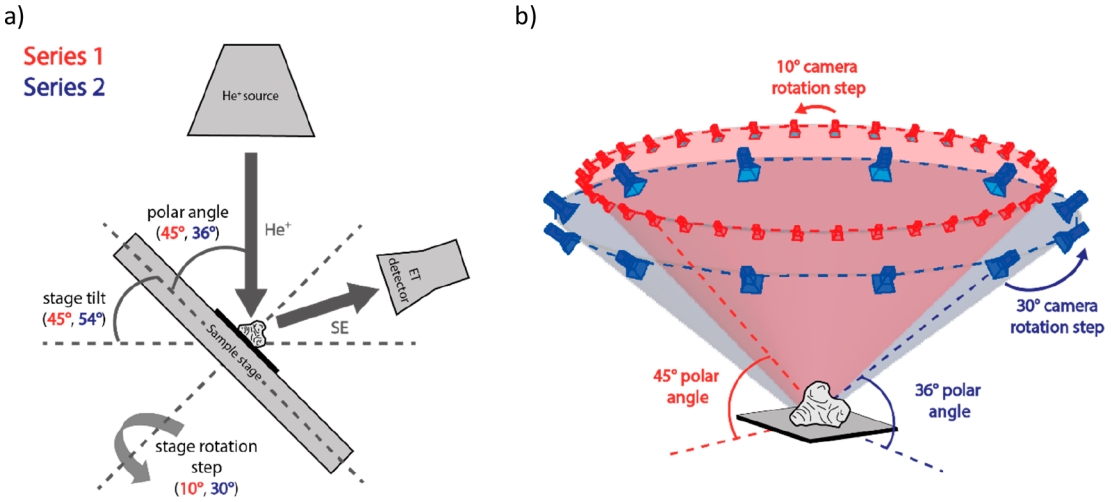

Figure 1. Sequential 2D SE image acquisition for 3D SE reconstruction. (a) The sample stage is tilted at 45° (i.e., 45° polar angle) and is rotated at 10° steps with SE image acquisitions in-between for a first SE image series (in red). In a second series (in blue), the process is repeated with a 54° stage tilt angle (i.e., 36° polar angle) and 30° rotation steps. In some cases, better results can be obtained by choosing image series at two different stage tilt (i.e., polar) angles while acquiring SE images with varying rotation angles. (b) The rotation process of the stage described in (a) is equivalent to a rotation of the camera (i.e., the He^+ source and the ET detector in the HIM) around the ROI at two different polar angles (Series 1 with red cameras: 45°, Series 2 with blue cameras: 36°) and rotation steps (Series 1:10°, Series 2:30°).

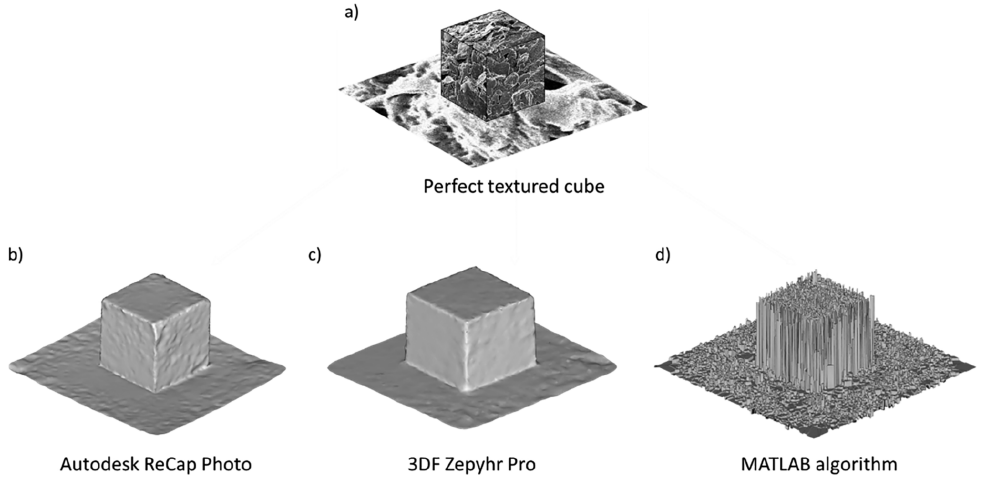

Figure 2. Photogrammetric 3D surface reconstructions from 36 images of a textured "perfect" cube on a base in (a) using the following software: (b) Autodesk ReCap Photo, (c) 3DF Zephyr Pro, and (d) a simulation algorithm created in MATLAB. Textures are not shown for the 3D reconstructions.

Nanofab HIM, which is equipped with an add-on SIMS system (therefore called "HIM-SIMS" instrument).[7] The primary beam (He^+ or Ne^+) is produced in a Gas Field Ion Source (GFIS) which consists of a cryogenically cooled sharp tip having an apex formed by only three atoms ("trimer"), acting as an ion source.[6] He (or Ne) atoms adsorbing on the tip are extracted and ionized by the high electric field applied between the tip and an extraction electrode. The ion beam is directed downward through the column to the sample. When impinging on the sample, the ions generate SE's emitted from the extreme surface, providing a high surface sensitivity. A spatial resolution of down to 0.5 nm is achieved using He^+.[7]

2.3. Photogrammetric 2D SE Image Acquisition. For 3D reconstruction using photogrammetry, 2D SE images were taken at well-defined positions, i.e., rotation and tilt angles of the stage allowing to record images all around the ROI (Figure 1a). This rotation of the stage is equivalent to a circular movement of the (He^+) source and the Everhart-Thornley (ET) detector around the ROI (Figure 1b). Optimal results were obtained by using a series of image acquisitions at a specific polar angle with respect to the sample surface (e.g., 45°) with small 10° stage rotation steps (in total 36 images for a complete turn). A series with another polar angle (e.g., 36°, equivalent to 54° stage tilt) at larger 30° rotation steps (in total 12 images) can be acquired in addition, because this can improve the reconstruction in certain cases,[18] where features located at slight overhangs of the ROI could not be registered at a 45° polar angle.

For both soil microaggregates, SE images were acquired with a 20 keV He^+ ion beam of 0.5 pA for a frame of 1024 × 1024 pixels using an average of 4 lines at 10 μs/pixel (Field of View (FOV) of 20 μm for the SE image series). The first presented soil microaggregate was reconstructed using 39 SE images (image acquisition every 15° at 45° tilt and every 24° at 54° tilt) and the second one using 35 SE images (image acquisition every 10° at 45° tilt).

https://doi.org/10.1021/acs.est.1c02971
Environ. Sci. Technol. 2021, 55, 9384−9393

2.4. Photogrammetric 3D SE Reconstruction. Three-dimensional reconstructions presented here were obtained using the software Autodesk ReCap Photo,[32] but were also reconstructed with 3DF Zepyhr Pro[33,34] for testing and comparison purposes. In Autodesk, images are simply implemented without having the possibility to play on internal parameters and influence on the final result. In 3DF Zephyr Pro, the reconstruction is done step-by-step by the user, i.e., search for features, matches in images, alignment of the camera positions, reconstruction of a dense point cloud, formation of a mesh, and finally addition of a colored texture.[34] Additionally, internal camera parameters (focal length, distortion, and optical center) can be implemented or chosen to be determined automatically.[35] In both software packages, the outcome is a textured 3D model which can be studied at all possible angles and magnifications.

For the first soil microaggregate, in total 24 906 data points were created ("vertices"), while for the second one, 55 094 vertices were reconstructed.

2.5. Ground Truth Comparison. In order to have an enhanced estimation of the reconstruction accuracy in general and potential issues related to the reconstruction process, a simplified mathematical algorithm for 3D reconstruction from 2D images was created in MATLAB proceeding in a comparable way step-by-step for the 3D reconstruction as for the commercial solutions. However, the fundamental difference between the algorithm and the commercial software is that the exact positions of the cameras are implemented by the user while for the commercial solutions a camera position estimation is performed.

Reconstructions of a cube were performed for the commercial software and the simulation algorithm and compared to the "perfect" cube ("ground truth comparison"). Therefore, a virtual cube was created in a 3D space and in total 36 images were taken around it at defined "camera" positions (45° polar angle and 10° azimuthal rotation step). The cube surface was textured to ensure a high amount of features and therefore to simplify the reconstruction process. The images were implemented into the simulation algorithm and both commercial software (Autodesk ReCap Photo and 3DF Zephyr Pro) to create a 3D model (Figure 2). In order to determine potential size-related shrinkages of the reconstructed structures, a cuboid was aligned to their shape. The cuboid height, length, and width were determined, while the deviation from the length and width from the cuboid height were calculated in %. The deviations using Autodesk ReCap Photo were 1.5% for the cuboid length and 2.5% for the width and using 3DF Zephyr Pro 25.1% (length) and 24.3% (width). The reconstruction using the simulation algorithm, though presenting a high amount of surface noise, gave an overall close to 0% deviation for both length and width.

The relatively high deviations for the commercial software can be explained in this case by an erroneous camera position estimation leading to local shrinkages and distortions in the 3D reconstructions, while the exact camera positions were implemented into the simulation algorithm. Structural deformations during the noise reduction and mesh reconstruction processes can not be excluded as well. However, in general the commercial software provides a more efficient and practical solution than the created simulation algorithm. Satisfactory 3D reconstructions with appropriate noise reduction, sharp edges, and smooth mesh reconstruction were obtained for both Autodesk ReCap and 3DF Zephyr Pro in less than 15 min, while the simulation algorithm needs approximately 1 h for the reconstruction and a smooth mesh creation still remains challenging due to the high amount of surface noise. Additionally, during the acquisition of serial SE images in the HIM around a ROI, a recentering of the sample stage onto the ROI is done resulting in a slight deviation from the actually designated "camera" positions of the SE image series. However, the MATLAB algorithm requires an exact implementation of the "camera" positions. Therefore, for SE images a "camera" position estimation as performed in the commercial solutions is still necessary to obtain a meaningful 3D reconstruction.

In summary, the commercial software provides satisfactory and high-quality 3D models, but possible local distortions due to an inaccurate camera position estimation should still be kept in mind. The resulting 3D reconstructions are available in the Supporting Information section.

2.6. Secondary Ion Mass Spectrometry (SIMS). Two different SIMS systems were used in the two presented analyses to take advantage of their unique capabilities. Before the analyses, the samples were covered by a 15 nm gold coating to reduce the charging effect during HIM-SIMS or NanoSIMS 50L acquisitions.

In the first case, the HIM add-on SIMS system (mentioned in 2.2) was used to allow in situ chemical imaging of the microaggregate's mineral phase at an ultrahigh spatial resolution. After imaging with HIM, we inserted the retractable secondary ion extraction box between the GFIS column and the sample and performed analytical SIMS measurements. Secondary ions were collected and transferred to the magnetic sector SIMS analyzer where up to four masses can be analyzed simultaneously.[8] A spatial resolution in SIMS imaging mode of sub 20 nm is reached for both, positive and negative ions, and a mass resolution of $m/\Delta m \approx 400$. The Ne^+ primary beam at normal incidence (25 keV, 2.5 pA) was used due to higher sputtering yields than with He^+ and therefore enhanced secondary ion signals,[36] while the secondary ions ^{23}Na, ^{24}Mg, and ^{39}K were imaged in 512 × 512 pixels at 5 ms/pixel (FOV 25 μm).

Second, a CAMECA NanoSIMS 50L, offering a poorer lateral resolution (50 nm)[37] than the HIM-SIMS (<20 nm), but a higher mass resolution for resolving compounds of organic carbon and nitrogen by depicting the distribution of specific isotopes (^{12}C, ^{13}C, ^{14}N, ^{15}N)[31] prone to mass interferences, was employed.

The Cs^+ ion beam (16 keV, 2 pA) of the NanoSIMS 50L instrument was used to image the spatial distribution of OM and mineral phases (256 × 256 pixels, 1 ms/pixel, sum over 65 planes per image, FOV 15 μm) by recording the negatively charged clusters $^{12}C^{12}C^-$, $^{12}C^{13}C^-$, $^{12}C^{14}N^-$, $^{12}C^{15}N^-$, and $^{27}Al^{16}O^-$ simultaneously at appropriate mass resolving power.

Thus, the choice of the HIM-SIMS instrument is motivated by the exploration of the spatial resolution to elucidate the soil mineral phase, whereas the NanoSIMS 50L thanks to its mass resolution and in combination with HIM offers an effective tool to study in depth OM distribution on mineral surfaces.

2.7. 4D Reconstruction. The SIMS images were projected onto their corresponding 3D SE surface representation using MeshLab.[38] MeshLab is a free and open source software for 3D visualization and analysis. Mutual points between the 2D SIMS image and the 3D SE representation were chosen manually ("2D-3D correspondences").[39] The 2D SIMS image was then aligned to the 3D SE representation with respect to

https://doi.org/10.1021/acs.est.1c02971
Environ. Sci. Technol. 2021, 55, 9384−9393

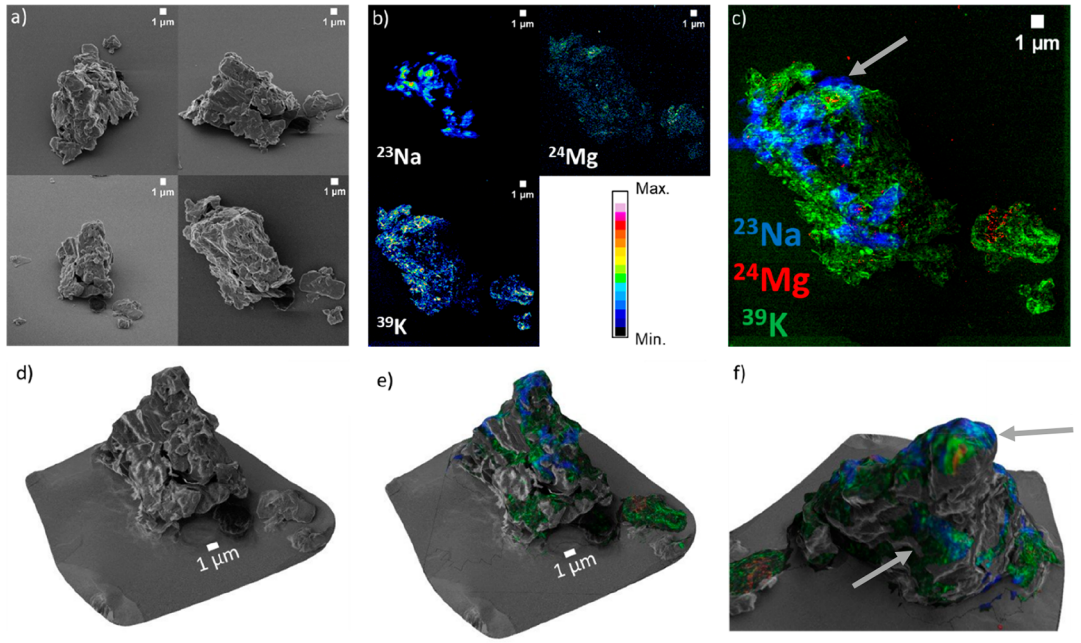

Figure 3. Workflow for a 4D reconstruction of a soil microaggregate. (a) Exemplary SE images: the upper images were acquired at 45° polar angle (45° stage tilt), while the rotation angles were 0° (top left) and 90° (top right). The lower left image corresponds to 36° polar angle (54° stage tilt) and 168° rotation and the lower right image was taken at normal incidence with respect to the wafer (i.e., polar angle 90°, stage tilt 0°). (b) SIMS images of ^{23}Na, ^{24}Mg, and ^{39}K. The scale bar indicates the secondary ion signal intensity for each mass. c) RGB SIMS composite image (Blue: ^{23}Na, Red: ^{24}Mg, Green: ^{39}K). d) 3D reconstruction of 39 SE images. (e) Projection of the RGB SIMS image from (c) onto the 3D SE representation from (d). In (d) and (e) the 3D, respectively, 4D model are shown at a view from a polar angle of 45°. (f) Zoomed view on the 4D reconstruction with an azimuthal rotation of 180° with respect to the view in (e). The arrow in (c) points to parts of the microaggregate which seem to be adjacent, but are actually vertically split as indicated by the two arrows in (f).

these correspondences. The image was projected onto the 3D representation and a texture map was created. Black pixels from this texture were removed since no secondary ions were detected there. The SIMS texture map generated in MeshLab was added to the texture map created from the SE images during the 3D reconstruction with a transparency of typically 60%. Hence, the final textured 4D representation allows one to observe topographical information from HIM and chemical information from SIMS throughout the reconstruction. Parts from the 3D representation where no SIMS signal was acquired, e.g., below overhangs ("shadow effect") or simply not containing the analyzed ion species, remain with only the topography texture.

3. RESULTS AND DISCUSSION

3.1. Methodological Description of 4D Reconstruction. *3.1.1. 4D Reconstruction Workflow.* The 4D reconstruction process is demonstrated stepwise in Figure 3. 39 SE images acquired in a series were used for this. Textured 3D meshes and animations of the soil microaggregate are available in the Supporting Information (SI) section.

Figure 3a illustrates three exemplary SE images used for the 3D reconstruction process taken at different stage tilt and rotation angles, while the lower right SE image was taken in top view. The topographical architecture of the soil microaggregate is enlightened at an unprecedented spatial resolution. The SIMS analysis shown in Figure 3b,c indicates a heterogeneous distribution of the mapped sodium (^{23}Na), magnesium (^{24}Mg), and potassium (^{39}K) on the same particle, as indicators for the mineral phase.

The chemical RGB SIMS image (Figure 3c) aligned and projected onto the 3D SE representation (Figure 3d) provides for the first time to our knowledge, the full 4D surface reconstruction of a soil microaggregate (Figure 3e). Figure 3f shows the zoomed-in 4D reconstruction with a 180° azimuthal rotation with respect to the representation in Figure 3e.

3.1.2. Reconstruction Evaluation and Recommendations. The overall convexity of the microaggregate favored a successful 3D SE reconstruction. The rough and inhomogeneous surface of the microaggregate (Figure 3a) facilitated the detection of a high number of features supporting the image matching process. However, pronounced topography is lacking on the Si wafer itself, which would favor in this case a flat representation of the wafer. Since features are missing on the Si wafer the software needs to interpolate the mesh over a long distance creating artifacts and erroneous unevenness on its surface.

As the working principle of common photogrammetry 3D reconstruction algorithms is based on feature detection and matching between images, ROI's with rough and inhomogeneous surfaces are rather easy to reconstruct. However, objects with a very smooth and featureless surface present a challenge for reconstruction using common photogrammetry software since the amount of detected and matched features in the images is extremely low.[20,40] Typically, images of macroscopic objects taken with an optical camera show a higher amount of detected features than SE images. The discrepancy of feature detection and matching amounts between optical and SE images is mainly due to the high amount of noise in SE images which can obstruct the feature detection algorithms considerably. Noise in the SE images can be reduced by increasing the number of average lines or frames during the image acquisition. Nevertheless, a compromise between time investment and improving image quality needs to be found.

https://doi.org/10.1021/acs.est.1c02971
Environ. Sci. Technol. 2021, 55, 9384−9393

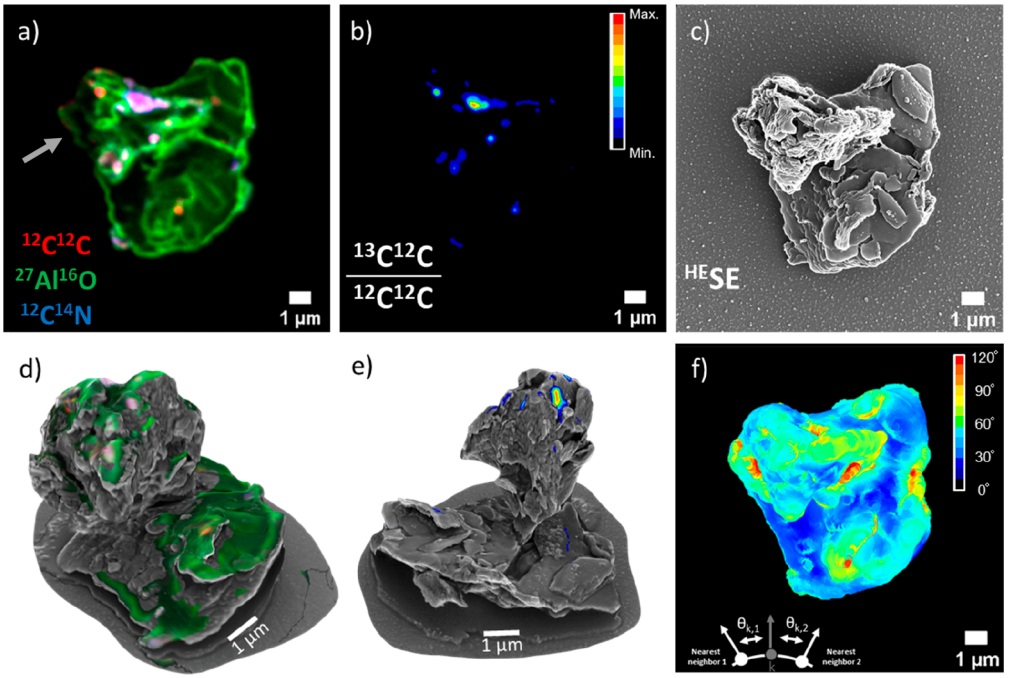

Figure 4. Topographic and compositional analysis of a soil microaggregate. (a) RGB SIMS image of the organic carbon and nitrogen compounds $^{12}C^{12}C$ (in red) and $^{12}C^{14}N$ (blue), and $^{27}Al^{16}O$ (green) representing the mineral phase of the microaggregate. The arrow points to an area with reduced secondary ion intensity resulting presumably from a restricted acceptance angle of the spectrometer. (b) Isotopic $^{13}C^{12}C/^{12}C^{12}C$ ratio image showing the areas enriched in ^{13}C. The scale bar indicates the ratio pixel intensity. (c) HIM 2D SE image in top view. The reaction of the implanted cesium with air led to the formation of little bubbles on the wafer of the Cs^+ irradiated area. (d) 4D surface reconstruction (side view at 45° polar angle) resulting from the overlay of the photogrammetric 3D SE reconstruction using 35 SE images and the RGB SIMS image from (a). (e) 4D surface reconstruction where the colored areas show the isotopic enrichment information from (b) (side view at 45° polar angle, 180° azimuthal rotation with respect to (d). (f) Visualization of the local particle's curvature determined from the average angles between the surface normal vectors of the considered nearest neighbors (top view). The curvature of the wafer was arbitrarily set to 0° in this representation. The scheme on the lower left side of (f) illustrates the determination of the local curvature: nearest neighbors i (1 and 2 in the scheme) of a 3D point k (in gray) are located first, then angles between their normal vectors $\theta_{k,i}$ and finally their average value is calculated.

Preliminary 3D SE reconstruction tests showed that on average at least 60 features should be detected per image and around 40 matches for consecutive images should be found to allow a meaningful 3D SE reconstruction. For this reconstruction, on average 124 features were detected per SE image with on average 87 matches for sequential images in the 45° tilt acquisition series. If no or only a few features are detected throughout the ROI in the SE images, then the photogrammetry software will interpolate 3D points arbitrarily during the mesh reconstruction process resulting in an erroneous 3D SE representation. Hence, a high amount of features on the ROI and minor defects surrounding the ROI (i.e., on the wafer) will simplify the feature detection and leads to a more authentic 3D SE reconstruction.

It is worth noticing that, although the number of detected and matched features might be high, camera positions can be estimated inaccurately leading to a distorted result. In this case, additional trials with manual changes of the internal camera parameters, i.e., focal length, lens distortion, and optical center might help to improve the result.

In fact, while common photogrammetry software is specialized in 3D reconstruction from optical camera images, no information about camera intrinsics is stored in SE images, i.e., focal distance, optical center, and lens distortion.[19] Therefore, an automatic calibration algorithm estimates the camera intrinsics and positions (i.e., the positions where the images were taken with respect to the object) from feature detection and matching among the images.[35] Hence, even if a high number of features were detected and matched in an image series, the resulting 3D SE representation can still be distorted or erroneous due to an incorrect determination of camera intrinsic parameters.

In the case of the 3D SE reconstruction in Figure 3d, the "camera" positions estimated by Autodesk ReCap Photo were generally in accordance with the designated "camera" positions defined by the stage tilt and rotations steps, hence an indicator for an authentic 3D reconstruction.

3.1.3. Advantages of 3D SE and SIMS Overlay. In Figure 3e, the SIMS image covers only areas of the particle where secondary ions were detected. Hence, small overhangs or areas, where no elements of interest could be detected, although subjected to the primary Ne^+ beam, e.g., the wafer or surrounding particles, remain in the SE texture exclusively. This can be well observed in Figure 3f: the top and some of the lower parts of the particle are covered with the SIMS information (indicated with two arrows), while the areas in-between present only the SE texture.

Thus, the superposition of the 3D SE model and SIMS images provides a more complete picture of an ROI compared to simple 2D images, because this representation of the SIMS information takes into account vertical ROI offsets. For instance, while in Figure 3c for the area indicated by the arrow, it seems that the secondary ion signal originates from adjacent parts of the microaggregate, in Figure 3f it becomes visible that this area is actually vertically split in space by areas

https://doi.org/10.1021/acs.est.1c02971
Environ. Sci. Technol. 2021, 55, 9384−9393

(marked with two arrows), where no secondary ions were detected due to their concave topography.

3.2. Applications of 4D Reconstruction for SIMS Analyses. *3.2.1. Imaging and Surface Reconstruction.* A more fundamental topographic analysis enabled by the 4D reconstruction is demonstrated on a 3D architecture of a soil microaggregate imaged using 35 HIM SE images superposed with the analytical information acquired with the NanoSIMS 50L. For the 3D SE reconstruction (available in the SI), on average 219 features were detected per SE image and 145 matches were found from one image to the next one in the series, indicating a more than sufficient amount of reconstructed 3D points for the surface model (see discussion in section 3.1.2). The reaction of the implanted cesium with air after the NanoSIMS 50L measurement[41] led to the creation of numerous spots all around the microaggregate, firmly supporting the feature detection and matching process on the wafer. Moreover, most of the "camera" positions calculated by the photogrammetry software were in agreement with the chosen stage tilt and rotation steps, i.e., no major distortions in the 3D model due to erroneous "camera" position estimations are assumed.

Analytical SIMS maps of $^{27}Al^{16}O$ (mineral phase), respectively $^{12}C^{12}C$ and $^{12}C^{14}N$ (organic matter), were acquired and combined into a single RGB image in Figure 4a (red: $^{12}C^{12}C$, green: $^{27}Al^{16}O$, blue: $^{12}C^{14}N$). The reduced secondary ion intensity on the upper left corner of the particle (marked with an arrow) in Figure 4a results presumably from a shadowing effect due to a restricted acceptance angle of the spectrometer.[18]

The $^{13}C^{12}C/^{12}C^{12}C$ ratio image was created and thus demonstrates areas enriched in ^{13}C on the surface of the microaggregate (Figure 4b).

A HIM SE acquisition was taken in the top view, i.e., at a normal incidence of the primary beam with respect to the wafer (Figure 4c). The formation of the above-mentioned spots spread on the wafer all around the microaggregate emerging after the Cs^+ irradiation can be well observed here.

4D surface reconstructions were compiled by performing the alignment and overlay between the reconstructed 3D SE model and first the RGB SIMS image (Figure 4d) and second the isotopic ratio information (Figure 4e). The representation of the SIMS information on the 3D SE surface model in Figure 4d,e, as discussed in section 3.1.3, represents an enhanced visualization of the SIMS information as the vertical distance between all the OM hotspots becomes visible.

3.2.2. Organic Matter 3D Distribution. On the basis of the 3D architecture model of the soil microaggregate a topographical analysis in relation to the distribution of the OM was performed. With this investigation, we intend to trace the inherent OM and the new OM, coming from isotopic labeling experiments, to better understand biogeochemical processes at the microscale.[37]

For the analysis of the 4D model, the surface curvature was used as a metric for topography variations,[42] since it allows one to characterize the microaggregate's topographical structure and distinguish between plain surfaces and local slopes, resulting from, e.g., micropores, cracks, or edges, and relate this information directly to the local chemical composition. The reconstructed surface model from Figure 4d was imported as a color-coded point cloud into MATLAB.

For the reconstructed microaggregate (counting only the reconstructed soil material and neglecting the wafer), a total surface of 197 μm^2 and a density of around 230 data points per μm^2 were measured. Hence, to estimate the local curvature for each 3D data point of the point cloud, 230 nearest neighbors for each 3D point were first determined. Additionally, by inspection of the point cloud, the consideration of 230 nearest neighbors per 3D point were assumed to be reasonable for a curvature calculation considering the density of the reconstructed point cloud and the overall microaggregate model size. Local surface normal vectors were computed and stored for each 3D point.

The local curvature σ_k for each 3D point k was then calculated with respect to its closest neighbors using the following definition:[42]

$$\sigma_k := \frac{1}{N}\sum_{i=1}^{N}\theta_{k,i} \tag{1}$$

where N is the number of considered nearest neighbors (here 230) and $\theta_{k,i}$ is the angle between the normal vector of 3D point k and the normal vector of the i^{th} nearest neighbor. In other words, the local curvature σ_k represents thus the average angle between the normal vector in the 3D point k and all the nearest neighbors' normal vectors. A color-coded visualization of the microaggregate's surface curvature is shown in the top view in Figure 4f.

The chemical information from the overlay of the 3D SE model and the RGB SIMS image (red: $^{12}C^{12}C$, green: $^{27}Al^{16}O$, blue: $^{12}C^{14}N$) was then associated with each 3D data point, in addition to the curvature information. The grayscale information from the SE was excluded for this analysis. The curvature σ_s for a specific ion species s (e.g., $^{12}C^{12}C$) is then defined as the average of all the curvatures of 3D points containing the ion species s:

$$\sigma_s := \frac{1}{n}\sum_{j=1}^{n}\sigma_{s,j} \tag{2}$$

where n is the number of all the 3D data points containing the ion species s and $\sigma_{s,j}$ is the curvature of a 3D point j, calculated previously using (1), containing chemical information on species s. For the 3D points containing $^{27}Al^{16}O$, we took only plain areas of the microaggregate into account to estimate the "background" curvature for the mineral phase, distributed throughout the entire microaggregate. The $^{27}Al^{16}O$ distribution nicely represents the clay minerals in such a sample, and thus the major component of these soil microaggregates. We found that the curvature $\sigma^{^{27}Al^{16}O}$ for all the 3D data points containing $^{27}Al^{16}O$ (mineral phase) for plain areas corresponded to 14.1°, while for 3D points presenting $^{12}C^{12}C$ and $^{12}C^{14}N$, showing OM distributed as hotspots, the curvatures $\sigma^{^{12}C^{12}C}$ and $\sigma^{^{12}C^{14}N}$ were 37.4° and 38.5°, respectively. Interestingly, by performing the same analysis on the 4D model from Figure 4e, the areas in the microaggregate enriched with ^{13}C, presented a very similar average curvature value $\sigma^{^{13}C^{12}C/^{12}C^{12}C}$, namely 37.2°. The standard deviation of the curvature for $^{27}Al^{16}O$ was around 4° and for the OM compounds close to 10° in each case.

Thus, for this soil microaggregate, the OM deposited on areas characterized on average by almost triple of the surface curvature compared to mineral plains of the microaggregate. This demonstrates that in the case of the studied microaggregate areas with low topography but also areas with high topography (highly curved), e.g. edges, in the microaggregate's mineral phase show no freshly added OM as indicated by the

https://doi.org/10.1021/acs.est.1c02971
Environ. Sci. Technol. 2021, 55, 9384−9393

absence of ^{13}C. Isotopically enriched OM, originating from the amendment of ^{13}C enriched substrates in the incubation experiment, were associated with the microaggregate surfaces on average in areas with a very similar surface curvature as the preexisting OM in the microaggregate.

Results show that topography and chemical composition are drivers of soil OM distribution which is in accordance with the findings of previous studies on soil organo-mineral structures.[37]

3.3. An Imaging Approach Extending Our Conceptual Understanding of Organo-Mineral Associations. *3.3.1. Benefits for Soils.* The microaggregate in Figure 3e, originating from the wet deposition sample preparation procedure, demonstrates the architecture of soil microaggregates as composed of distinct minerals with different chemical composition at a nonprecedent spatial resolution. This high spatial resolution is crucial to correlate the fate of OM with the buildup of microaggregates and thus mineral-associated OM. The mineral skeletal structure of the microaggregate and thus the mineral phase is represented by the ^{23}Na, ^{24}Mg, and ^{39}K distributions (Figure 3b). The spatial distribution of sodium, magnesium, and potassium demonstrates distinctly different microscale patterns that clearly resemble the different primary and pedogenic minerals that make up the microaggregate. As illite, chlorite, quartz, and kaolinite are the main mineral constituents of this soil material (data not shown), we demonstrate that the resembled structures represent these clay-sized minerals differentiated by the distinct proportion of the measured elements.

For the analysis of the microaggregate obtained by dry sieving, the 3D SE surface reconstruction in Figure 4d and the corresponding $^{27}Al^{16}O$ (Figure 4a) SIMS information greatly enhances the view on the soil microstructure as it correlatively visualizes the soil mineral phase and its positioning in the 3D arrangement of the microaggregate architecture. By combining the demonstrated correlation with the microscale distribution of OM phases from chemical images representing carbon and nitrogen, the 3D reconstruction allows one to differentiate between specific mineral particles vs microscale physical structure (surface curvature) for the association of OM with the mineral surfaces.

Thus, the demonstrated approach offers the potential to elucidate how chemical surface properties and physical microscale soil structure foster the formation of mineral associated OM. It allows one to correlate distinct soil mineral species with their specific function in the context of the microaggregate architecture at the relevant scale for biogeochemical processes.

3.3.2. Perspectives. The methodology of 4D surface reconstruction combining 3D topography and 1D analytical information obtained by EM and SIMS has been extended and applied successfully in soil biogeochemistry. In contrast to a traditional 2D image, our representation shows the specimen in its entirety and its surface topography information can be used to correlate it directly with the local chemical composition, which allows one to greatly enhance the conceptual view on soil microaggregate architecture and function. Thus, we were able to demonstrate that organo-mineral associations mainly form at medium curvatures pointing to specific surface properties of microaggregates that foster the formation of mineral-associated OM. Both inherited and freshly added OM is recovered at comparable topographic positions on the microaggregate.

The established approach provides the framework for detailed microstructural analyses of biogeochemical samples, reaching from soils to sediments. For applications in soil biogeochemistry, 4D reconstructions offer the possibility to delineate topographic (e.g., surface curvature) and chemical properties of mineral and organic particles including microaggregates that determine the cycling and distribution of for instance organo-mineral associated OM or microbial OM at the relevant process scale.

Finally, 4D reconstruction is not limited to the mentioned analysis techniques (HIM-SIMS, HIM-NanoSIMS 50L) but can be used more generally for correlative microscopy combining 3D topography (e.g., optical microscopy, electron microscopy) and analytical information (e.g., time-of-flight SIMS, X-ray photoelectron, or Raman spectroscopy) for mapping the distribution of chemical components inside the sample.

■ ASSOCIATED CONTENT

Supporting Information

The Supporting Information is available free of charge at https://pubs.acs.org/doi/10.1021/acs.est.1c02971.

Ground truth comparison, including File S1, 3D reconstruction of the cube with Autodesk ReCap Photo (.stl); File S2, 3D reconstruction of the cube with 3DF Zephyr Pro (.stl); and File S3, 3D reconstruction of the cube with the MATLAB simulation algorithm (.stl); *methodological description of 4D reconstruction*, including File S4, video (.avi format) of rotating 3D SE representation of the soil microaggregate; File S5, 3D SE model of the soil microaggregate (.obj) with corresponding texture (.jpg) and material file (.mtl); File S6, video (.avi) of rotating 4D reconstruction of the soil microaggregate; and File S7, 4D model of the soil microaggregate (.obj) with corresponding texture (.jpg) and material file (.mtl); and *applications of 4D reconstruction for SIMS analyses*, including File S8, video (.avi format) of rotating 3D SE representation of the soil microaggregate; File S9, 3D SE model of the soil microaggregate (.obj) with corresponding texture (.jpg) and material file (.mtl); File S10, video (.avi) of rotating 4D reconstruction of the soil microaggregate (organic matter: 12C, 14N), File S11, 4D model of the soil microaggregate (.obj) with corresponding texture (.jpg) and material file (.mtl) (organic matter: 12C, 14N), File S12, video (.avi) of rotating 4D reconstruction of the soil microaggregate (ratio $^{12}C^{13}C/^{12}C^{12}C$), and File S13, 4D model of the soil microaggregate (.obj) with corresponding texture (.jpg) and material file (.mtl) (ratio $^{12}C^{13}C/^{12}C^{12}C$) (ZIP)

Description of the SI files (PDF)

■ AUTHOR INFORMATION

Corresponding Author

Alexander D. Ost − *Advanced Instrumentation for Nano-Analytics (AINA), Materials Research and Technology Department (MRT), Luxembourg Institute of Science and Technology (LIST), 4422 Belvaux, Luxembourg; University of Luxembourg, 4365 Esch-sur-Alzette, Luxembourg;* Present Address: Luxembourg Institute of Science and Technology (LIST), L-4422 Belvaux, Luxembourg.;

https://doi.org/10.1021/acs.est.1c02971
Environ. Sci. Technol. 2021, 55, 9384−9393

orcid.org/0000-0002-7465-2541; Phone: +352 275 888 3550; Email: alexander.ost@list.lu

Authors

Tianyi Wu − *Soil Science, TUM School of Life Sciences, Technical University of Munich, 85354 Freising, Weihenstephan, Germany*

Carmen Höschen − *Soil Science, TUM School of Life Sciences, Technical University of Munich, 85354 Freising, Weihenstephan, Germany*

Carsten W. Mueller − *Department of Geosciences and Natural Resource Management Geography, University of Copenhagen, 1350 Copenhagen, Denmark*

Tom Wirtz − *Advanced Instrumentation for Nano-Analytics (AINA), Materials Research and Technology Department (MRT), Luxembourg Institute of Science and Technology (LIST), 4422 Belvaux, Luxembourg*

Jean-Nicolas Audinot − *Advanced Instrumentation for Nano-Analytics (AINA), Materials Research and Technology Department (MRT), Luxembourg Institute of Science and Technology (LIST), 4422 Belvaux, Luxembourg;* orcid.org/0000-0002-4966-7653

Complete contact information is available at: https://pubs.acs.org/10.1021/acs.est.1c02971

Notes

The authors declare no competing financial interest.

■ ACKNOWLEDGMENTS

The authors gratefully acknowledge support by the Luxembourg National Research Fund (FNR) under grant no. INTER/DFG/17/11779689, and the Deutsche Forschungsgemeinschaft (DFG) through grant no. HO 5121/1-1.

■ REFERENCES

(1) Wirtz, T.; Philipp, P.; Audinot, J. N.; Dowsett, D.; Eswara, S. High-resolution high-sensitivity elemental imaging by secondary ion mass spectrometry: From traditional 2D and 3D imaging to correlative microscopy. *Nanotechnology* **2015**, *26*, 434001.

(2) Vollnhals, F.; Audinot, J. N.; Wirtz, T.; Mercier-Bonin, M.; Fourquaux, I.; Schroeppel, B.; Kraushaar, U.; Lev-Ram, V.; Ellisman, M. H.; Eswara, S. Correlative Microscopy Combining Secondary Ion Mass Spectrometry and Electron Microscopy: Comparison of Intensity-Hue-Saturation and Laplacian Pyramid Methods for Image Fusion. *Anal. Chem.* **2017**, *89*, 10702−10710.

(3) Hollricher, O.; Schmidt, U.; Breuninger, S. RISE Microscopy: Correlative Raman-SEM Imaging. *Microsc. Today* **2014**, *22*, 36−39.

(4) Reddick, L. E.; Alto, N. M. Correlative light and electron microscopy (CLEM) as a tool to visualize microinjected molecules and their eukaryotic sub-cellular targets. *J. Visualized Exp.* **2012**, 1.

(5) Moore, K. L.; Lombi, E.; Zhao, F. J.; Grovenor, C. R. M. Elemental imaging at the nanoscale: NanoSIMS and complementary techniques for element localisation in plants. *Anal. Bioanal. Chem.* **2012**, *402*, 3263−3273.

(6) Wirtz, T.; De Castro, O.; Audinot, J. N.; Philipp, P. Imaging and Analytics on the Helium Ion Microscope. *Annu. Rev. Anal. Chem.* **2019**, *12*, 523−543.

(7) Hlawacek, G.; Gölzhäuser, A. *Helium Ion Microscopy*; Springer Nature: Basel, Switzerland, 2016 DOI: 10.1007/978-3-319-41990-9.

(8) Dowsett, D.; Wirtz, T. Co-Registered in Situ Secondary Electron and Mass Spectral Imaging on the Helium Ion Microscope Demonstrated Using Lithium Titanate and Magnesium Oxide Nanoparticles. *Anal. Chem.* **2017**, *89*, 8957−8965.

(9) Williams, P. Secondary Ion Mass Spectrometry. *Annu. Rev. Mater. Sci.* **1985**, *15*, 517−548.

(10) Zalm, P. Secondary ion mass spectrometry. *Vacuum* **1994**, *45*, 753−772.

(11) van der Heide, P. *Secondary Ion Mass Spectrometry*; John Wiley & Sons, Inc.: Hoboken, NJ, 2014 DOI: 10.1002/9781118916780.

(12) Gillen, G.; Fahey, A.; Wagner, M.; Mahoney, C. 3D molecular imaging SIMS. *Appl. Surf. Sci.* **2006**, *252*, 6537−6541.

(13) Wucher, A.; Cheng, J.; Winograd, N. Protocols for Three-Dimensional Molecular Imaging Using Mass Spectrometry. *Anal. Chem.* **2007**, *79*, 5529−5539.

(14) Koch, S.; Ziegler, G.; Hutter, H. ToF-SIMS measurements with topographic information in combined images. *Anal. Bioanal. Chem.* **2013**, *405*, 7161−7167.

(15) Terlier, T.; Lee, J.; Lee, K.; Lee, Y. Improvement of the Correlative AFM and ToF-SIMS Approach Using an Empirical Sputter Model for 3D Chemical Characterization. *Anal. Chem.* **2018**, *90*, 1701−1709.

(16) Fleming, Y.; Wirtz, T.; Gysin, U.; Glatzel, T.; Wegmann, U.; Meyer, E.; Maier, U.; Rychen, J. Three dimensional imaging using secondary ion mass spectrometry and atomic force microscopy. *Appl. Surf. Sci.* **2011**, *258*, 1322−1327.

(17) Akhtar, I.; Rehman, M. A.; Choi, W.; Kumar, S.; Lee, N.; Cho, S. J.; Park, H. H.; Park, K. H.; Seo, Y. Three-dimensional atomic force microscopy for ultra-high-aspect-ratio imaging. *Appl. Surf. Sci.* **2019**, *469*, 582−592.

(18) Vollnhals, F.; Wirtz, T. Correlative Microscopy in 3D: Helium Ion Microscopy-Based Photogrammetric Topography Reconstruction Combined with in situ Secondary Ion Mass Spectrometry. *Anal. Chem.* **2018**, *90*, 11989−11995.

(19) Eulitz, M.; Reiss, G. 3D reconstruction of SEM images by use of optical photogrammetry software. *J. Struct. Biol.* **2015**, *191*, 190−196.

(20) Gontard, L. C.; Schierholz, R.; Yu, S.; Cintas, J.; Dunin-Borkowski, R. E. Photogrammetry of the three-dimensional shape and texture of a nanoscale particle using scanning electron microscopy and free software. *Ultramicroscopy* **2016**, *169*, 80−88.

(21) Hartley, R.; Zisserman, A., Eds.; *Multiple View Geometry in Computer vision*, 2nd ed.; Cambridge University Press: Cambridge, 2004 DOI: 10.1017/CBO9780511811685.

(22) Peter Heng, B. C.; Chandler, J. H.; Armstrong, A. Applying close range digital photogrammetry in soil erosion studies. *Photogramm. Rec.* **2010**, *25*, 240−265.

(23) Spampinato, V.; Dialameh, M.; Franquet, A.; Fleischmann, C.; Conard, T.; Van Der Heide, P.; Vandervorst, W. A Correlative ToF-SIMS/SPM Methodology for Probing 3D Devices. *Anal. Chem.* **2020**, *92*, 11413−11419.

(24) Tisdall, J. M.; Oades, J. M. Organic matter and water-stable aggregates in soils. *J. Soil Sci.* **1982**, *33*, 141−163.

(25) Edwards, A. P.; Bremner, J. M. Microaggregates in Soils. *J. Soil Sci.* **1967**, *18*, 64−73.

(26) Six, J.; Conant, R. T.; Paul, E. A.; Paustian, K. Stabilization mechanisms of soil organic matter: Implications for C-saturation of soils. *Plant Soil* **2002**, *241*, 155−176.

(27) Totsche, K. U.; Amelung, W.; Gerzabek, M. H.; Guggenberger, G.; Klumpp, E.; Knief, C.; Lehndorff, E.; Mikutta, R.; Peth, S.; Prechtel, A.; Ray, N.; Kögel-Knabner, I. Microaggregates in soils. *J. Plant Nutr. Soil Sci.* **2018**, *181*, 104−136.

(28) Chenu, C.; Plante, A. F. Clay-sized organo-mineral complexes in a cultivation chronosequence: Revisiting the concept of the "primary organo-mineral complex,. *Eur. J. Soil Sci.* **2006**, *57*, 596−607.

(29) IUSS Working Group WRB. *World Reference Base for Soil Resources—A Framework for International Classification, Correlation, and Communication*; FAO: Rome, 2006. https://research.wur.nl/en/publications/world-reference-base-for-soil-resources-2006-a-framework-for-inte.

(30) Felde, V.; Schweizer, S. A.; Biesgen, D.; Ulbrich, A.; Uteau, D.; Knief, C.; Graf-Rosenfellner, M.; Kögel-Knabner, I.; Peth, S. Wet sieving versus dry crushing: Soil microaggregates reveal different physical structure, bacterial diversity and organic matter composition in a clay gradient. *Eur. J. Soil Sci.* **2021**, *72*, 810.

(31) Mueller, C.W.; Weber, P.K.; Kilburn, M.R.; Hoeschen, C.; Kleber, M.; Pett-Ridge, J., Advances in the analysis of biogeochemical interfaces. *NanoSIMS to Investigate Soil Microenvironments*; Elsevier Inc., 2013 DOI: 10.1016/B978-0-12-407685-3.00001-3.
(32) ReCap Photo—Photogrammetry Guide, 2017. https://help.autodesk.com/sfdcarticles/attachments/ReCap_Photo-Photogrammetry_Guide_V1.pdf (accessed June 15, 2021).
(33) 3DFLOW 3DF Zephyr—User Manual, 2013 http://3dflow.net (accessed June 15, 2021).
(34) Marčiš, M.; Fraštia, M. Photogrammetric Measurement of a Wooden Truss. *Slovak J. Civ. Eng.* **2018**, *26*, 1−10.
(35) De la Escalera, A.; Armingol, J. M. Automatic chessboard detection for intrinsic and extrinsic camera parameter calibration. *Sensors* **2010**, *10*, 2027−2044.
(36) Pillatsch, L.; Vanhove, N.; Dowsett, D.; Sijbrandij, S.; Notte, J.; Wirtz, T. Study and optimization of SIMS performed with He+ and Ne+ bombardment. *Appl. Surf. Sci.* **2013**, *282*, 908−913.
(37) Vogel, C.; Mueller, C. W.; Höschen, C.; Buegger, F.; Heister, K.; Schulz, S.; Schloter, M.; Kögel-Knabner, I. Submicron structures provide preferential spots for carbon and nitrogen sequestration in soils. *Nat. Commun.* **2014**, *5*, 2947.
(38) Cignoni, P.; Callieri, M.; Corsini, M.; Dellepiane, M.; Ganovelli, F.; Ranzuglia, G. *MeshLab: An Open-Source Mesh Processing Tool*; Scarano, V. I., De Chiara, R., Erra, U., Eds.; *Eurographics Ital. Chapter Conf.*, 2008: pp 129−136 DOI: 10.2312/LocalChapterEvents/ItalChap/ItalianChapConf2008/129-136.
(39) Sottile, M.; Dellepiane, M.; Cignoni, P.; Scopigno, R. Mutual Correspondences: an Hybrid Method for Image-to-Geometry Registration. Puppo, E., Brogni, A., De Floriani, L., Eds.; *Eurographics Ital. Chapter Conf.*, 2010: pp 80−88. 10.2312/LocalChapterEvents/ItalChap/ItalianChapConf2010/081-088.
(40) Kudryavtsev, A., 3D Reconstruction in Scanning Electron Microscope: from image acquisition to dense point cloud. *Signal and Image Processing*; Université Bourgogne: Franche-Comté, 2017.
(41) Miethe, K.; Gries, W.H.; Pöcker, A. Ion Deposition Effects in and Around Sputter Craters Formed by Cesium Primary Ions. Benninghoven, A., Colton, R. J., Simons, D.S., Werner, H. W., Eds.; Second. *Ion Mass Spectrom*. SIMS V Springer: Berlin/Heidelberg, 1986; pp 347−349 DOI: 10.1007/978-3-642-82724-2_92.
(42) Wilke, W. *Segmentierung und Approximation großer Punktwolken*; Technical University of Darmstadt, 2002. http://tuprints.ulb.tu-darmstadt.de/255/.

https://doi.org/10.1021/acs.est.1c02971
Environ. Sci. Technol. 2021, 55, 9384−9393